Shear flow of active matter in thin channels

M. Carme Calderer
School of Mathematics, University of Minnesota, Minneapolis, Minnesota 55442, USA

Dmitry Golovaty and Lingxing Yao
Department of Mathematics, University of Akron, Akron, Ohio 44325, USA

Longhua Zhao
Department of Mathematics, Applied Mathematics and Statistics, Case Western Reserve University, Cleveland, Ohio 44106, USA

(Received 7 February 2021; revised 13 June 2021; accepted 6 July 2021; published 17 September 2021)

We study the shear flow of active filaments confined in a thin channel for extensile and contractile fibers. We apply the Ericksen-Leslie equations of liquid crystal flow with an activity source term. The dimensionless form of this system includes the Ericksen, activity, and Reynolds numbers, together with the aspect ratio of the channel, as the main driving parameters. We perform a normal mode stability analysis of the base shear flow. For both types of fibers, we arrive at a comprehensive description of the stability properties and their dependence on the parameters of the system. The transition to unstable frequencies in extensile fibers occurs at a positive threshold value of the activity parameter, whereas for contractile ones a complex behavior is found at low absolute value of the activity number. The latter might be an indication of the biologically relevant plasticity and phase transition issues. In contrast with extensile fibers, flows of contractile ones are also found to be highly sensitive to the Reynolds number. The work on extensile fibers is guided by experiments on active filaments in confined channels and aims at quantifying their findings in the prechaotic regime.

DOI: 10.1103/PhysRevE.104.034607

I. INTRODUCTION

We study laminar flow of active matter filaments confined to thin channels. We consider flows generated in both extensile and contractile fibers with a goal of comparing their stability behaviors and investigate how confinement affects both types of response. Our flow model is based on the Ericksen-Leslie equations of liquid crystals with an activity source term [1,2] added to represent both types of fibers. Following up on a previous study of extensile fibers [3], we analyze the mechanisms of instability of well-aligned shear flows with a linear velocity profile and quantitatively explore regimes of instability. We perform a normal mode analysis of the flow equations and find the instability thresholds of the uniformly aligned shear flow in terms of the relevant nondimensional parameter groups. Increased activity and Ericksen number are found to drive both extensile and contractile systems out of the stable regime, and we find significantly different stability profiles at low activity or channel width. We also find that the vorticity and speed of the perturbing flow increase as the activity number $\mathcal{A}$ increases. A numerical method based on the discretization of the linear system by Chebyshev polynomials is used in the normal mode stability analysis, specifically, in solving the underlying spectral problem. The outcome provides a comprehensive description of the stability profiles of both types of fibers in confinement, in terms of the frequency and speed of the perturbations, the activity, Ericksen, and Reynolds numbers, and the geometry of the channel.

Extensile fibers are known to form rodlike nematic liquid crystalline phases, due to their elongated molecular shapes. Contractile fibers typically consist of disk or planklike molecular groups that fall into the class of discotic nematic liquid crystals. Both types of fibers are well represented by a common liquid crystal model, although certain parameters, such as those relevant to shear flow, fall in different ranges. The type of extensile fibers that we refer to, characterized by $\mathcal{A} > 0$, consists of self-propelled elongated units formed by bundled microtubules that are powered by adenosine triphosphate (ATP)-consuming kinesin 29 [4,5]. Actin fibers are contractile, $\mathcal{A} < 0$, and show a behavior distinct from that of their extensile counterpart. The sign of the activity parameter emerges in connection with the terminology of *swimmers*, with extensile particles labeled *pushers* and contractile ones *pullers* as illustrated in Fig. 1 [6–9].

We aim at understanding the stability behavior of active matter in confinement. In particular, our work, at the rest state limit $|\mathcal{A}| \to 0$, provides a quantitative interpretation of the *generic instability* concept put forward by Ramaswamy and Rao [10] for active systems. This property also emerged in earlier theoretical work on extensile fibers finding that laterally confined active nematics undergo an instability of a spontaneous laminar flow when the channel width reaches a certain threshold value that depends on the strength of the activity [11]. These results were later confirmed in experiments with spindle-shaped cells [12]. *In vitro* actin fibers have a length of about 20 μm and diameter of 7 nm, forming bundles

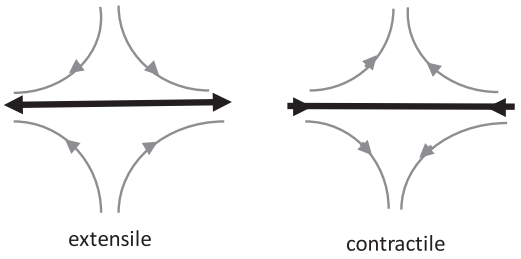

FIG. 1. Flow profile (gray curves) generated by extensile (left) and contractile fibers (right). The thick black arrow represents the nematic director, pointing along the rod axis in rodlike particles, and perpendicular to the disk in discotic ones.

with diameter of 50 nm. (The bundle size would increase, if crosslinking occurred [13].)

The Ericksen-Leslie equations of incompressible liquid crystal flow and their numerical simulations have been used in many studies of active systems, especially in the turbulent regimes [14]. The variables of the model include the velocity field $\boldsymbol{v}$, the pressure p associated with the incompressibility constraint, and the unit nematic director $\boldsymbol{n}$, representing the local average alignment of the system. The director field takes different significance for rodlike and discotic liquid crystals. In the former, it represents the average alignment of the rodlike constituent molecules, whereas for discotic, planklike molecular groups, $\boldsymbol{n}$ corresponds to the perpendicular direction to the planar structures. Since the flows that we study are plane, we formulate the problem in terms of the *stream function* Ψ.

The dimensionless form of the equations involves, in addition to the aspect ratio ℓ of the channel, three main parameter groups. Two of them—the Reynolds $\mathcal{R}_e$ and Ericksen $\mathcal{E}_r$ numbers—are defined in the same way as for passive flows. The activity parameter $\mathcal{A}$ quantifies the activity level in the system. This parameter has a different sign depending on whether the fibers are extensile or contractile. Although $\mathcal{R}_e$ is significantly smaller than other nondimensional parameters of the system, it influences its stability behavior in some subtle ways. $\mathcal{E}_r$ represents the ratio of the viscous to the elastic torques and may take very large values.

In this work, we focus on the plane shear flow of an active liquid crystal in the aligning regime. A signature feature of shear flow is the balance between the stretching and rotational effects of the flow, measured by λ, the shear aligning parameter. Aligning regimes are characterized by the dominance of the extensional effect over the rotating one and correspond to $|\lambda| > 1$ (for tumbling regimes $|\lambda| < 1$), respectively [8,15].

Several works on active liquid crystals found in the literature use the Beris-Edwards model based on the evolution of the order tensor Q rather than the director of the Ericksen-Leslie theory [16]. Q represents a symmetric, traceless second-order tensor whose two independent eigenvectors are the director fields of the theory. They reduce to a single eigenvector $\boldsymbol{n}$ in the uniaxial case, with Q admitting the representation $Q = s(\boldsymbol{n} \otimes \boldsymbol{n} - \frac{1}{3}I)$, where the scalar $s \in (-\frac{1}{2}, 1)$ corresponds to the single, independent eigenvalue. For rodlike liquid crystals, $s > 0$, whereas for discotic materials, $s \in (-\frac{1}{2}, 0)$. A theory of uniaxial liquid crystal flow based on the fields s and $\boldsymbol{n}$ was proposed by Ericksen [17], in order to account for defects of degree ± 1 and line defects. The theory resembles that of Beris-Edwards restricted to uniaxial order tensors (except for some rheological features). We also make partial use of the order parameter s in order to extract additional information about the system (see the Supplemental Material [18]).

We carry out a normal mode analysis of the shear flow, with ω representing the wave number of the perturbation and $\mathrm{Im}(c)$, with c representing the complex speed of the perturbation, the corresponding growth rate. A perturbation with wave number ω and $\mathrm{Im}(c) > 0$ is unstable, and otherwise, stable. The threshold $\mathrm{Im}(c) = 0$ represents the neutral stability threshold.

This paper is organized as follows. In the Background section, we give a brief survey of the classical Ericksen-Leslie system for passive liquid crystals and their modification to model active materials [1,2,19,20]. The associated free energy corresponds to the well-known model by Oseen, Frank, and Zöcher [21–23]. We illustrate how these equations are related to the more general models of Landau and de Gennes [24], coupled with the flow equations by Beris and Edwards [16,25]. When restricted to uniaxial materials, the latter give rise to Ericksen's model for liquid crystals with variable degree of orientation [17], for which we give an abridged description. In this section, we also present the dimensionless version of the equations of flow that serves to identify the relevant parameter groups of the system: the Ericksen, activity and Reynolds numbers, and the channel aspect ratio. The Ericksen number, representing the ratio of the viscous to the elastic torques, is a key parameter in studies of passive flow, with large values of that number being associated with relevant instabilities [15,26,27]. In the Models section, we develop the equations of plane shear flow, derive the equation of steady state at the core of the current work, and obtain the base solution with constant director angle. In the Methods section, we set up the class of perturbations of the uniformly aligned shear flow and the framework of its normal mode analysis. Furthermore, we present the numerical method to analyze the stability of the base shear flow and the stability results for contractile fibers and compare them with our earlier results on the extensile [3]. We also develop the mathematical tools to study flows with variable director field, relevant to future studies of higher activity systems. The Results and Discussion section presents all the findings of the work. In particular, it describes the properties of the uniformly aligned stationary state as well as those of the shear flow with variable director orientations. It proceeds with the full characterization of the stability behavior of the uniformly aligned base flow, in terms of the dimensionless parameters of the system, as obtained from the graphs of the wave number with respect to the activity parameter. Finally, we draw the conclusions.

The fully developed equations for the Ericksen-Leslie and Ericksen models are presented in the Supplemental Material [18]. A summary of the plots that resulted from the numerical simulations is also given there.

II. BACKGROUND

As for its passive counterpart, an active liquid crystal is assumed to be a viscous anisotropic and incompressible fluid with activity sources drawn from internal mechanisms or from the environment. We now present a survey of the liquid crystal equations as developed by Ericksen and Leslie [1,2,19,20,28]. Incorporating the mechanisms of activity as developed much later by Ramaswami *et al.* [9,10] yields the system known as *active liquid crystals*. Let $\Omega \subset \mathbb{R}^3$ be an open domain occupied by the liquid crystal with the smooth boundary $\partial\Omega$. The Ericksen-Leslie equations of balance of linear and angular momentum (upon taking the cross product with $\boldsymbol{n}$, and neglecting rotational inertia) and the incompressibility and unit director constraints for the velocity field $\boldsymbol{v}$, pressure p, and director field $\boldsymbol{n}$ in Ω and at time $t > 0$ are [2]

$$\rho\dot{\boldsymbol{v}} = \nabla \cdot \sigma, \tag{1}$$

$$\gamma_1 \dot{\mathbf{n}} \times \mathbf{n} = \nabla \cdot \left(\frac{\partial W_{\mathrm{OF}}}{\partial \nabla \mathbf{n}}\right) \times \mathbf{n} - \frac{\partial W_{\mathrm{OF}}}{\partial \mathbf{n}} \times \mathbf{n} + \gamma_1 \boldsymbol{\Omega}\mathbf{n} \times \mathbf{n} - \gamma_2 \mathbf{A}\mathbf{n} \times \mathbf{n}, \tag{2}$$

$$\nabla \cdot \boldsymbol{v} = 0, \quad \boldsymbol{n} \cdot \boldsymbol{n} = 1, \tag{3}$$

with $\rho > 0$ denoting the constant mass density. The function W_{OF} denotes the Oseen-Frank energy of the liquid crystal, quadratic in the gradients of $\boldsymbol{n}$:

$$W_{\mathrm{OF}}(\boldsymbol{n}, \nabla\boldsymbol{n}) = \tfrac{1}{2}\{k_1|\nabla \cdot \boldsymbol{n}|^2 + k_2|(\nabla \times \boldsymbol{n}) \cdot \boldsymbol{n}|^2 + k_3|(\nabla \times \boldsymbol{n}) \times \boldsymbol{n}|^2 + (k_2 + k_4)\nabla \cdot \times [(\boldsymbol{v} \cdot \nabla)\boldsymbol{n} - (\nabla \cdot \boldsymbol{n})\boldsymbol{n}]\}. \tag{4}$$

with k_1, k_2, $k_3 > 0$, $k_2 > |k_4|$, and $2k_1 \geqslant k_2 + k_4$ denote the Frank elastic constants. The total energy is

$$\mathcal{E} = \int_\Omega \left[\frac{1}{2}\rho\dot{\boldsymbol{v}} \cdot \dot{\boldsymbol{v}} + W_{\mathrm{OF}}(\boldsymbol{n}, \nabla\boldsymbol{n})\right] d\mathbf{x}.$$

The Cauchy stress tensor σ is the sum of the elastic, viscous $\hat{\sigma}$ and active σ_A components, respectively:

$$\sigma = -p\mathbf{I} - \nabla\mathbf{n}^T \frac{\partial W_{\mathrm{OF}}}{\partial \nabla \mathbf{n}} + \hat{\sigma} + \sigma_{\mathcal{A}}, \tag{5}$$

$$\hat{\sigma} = \alpha_1(\mathbf{n} \cdot \mathbf{A}\mathbf{n})\mathbf{n} \otimes \mathbf{n} + \alpha_2 \mathbf{N} \otimes \mathbf{n} + \alpha_3 \mathbf{n} \otimes \mathbf{N} + \alpha_4 \mathbf{A} + \alpha_5 \mathbf{A}\mathbf{n} \otimes \mathbf{n} + \alpha_6 \mathbf{n} \otimes \mathbf{A}\mathbf{n}, \tag{6}$$

$$\sigma_A = -a\,\mathbf{n} \otimes \mathbf{n}, \quad \text{with}$$
$$\mathbf{A} = \frac{\nabla\mathbf{v} + (\nabla\mathbf{v})^T}{2}, \ \boldsymbol{\Omega} = \frac{\nabla\mathbf{v} - (\nabla\mathbf{v})^T}{2}, \ \mathbf{N} = \dot{\mathbf{n}} - \boldsymbol{\Omega}\mathbf{n}. \tag{7}$$

Here the superimposed dot denotes the material time derivative, that is, $\dot{f}(t, \boldsymbol{x}) = \frac{\partial f}{\partial t} + (\boldsymbol{v} \cdot \nabla)f$. The Leslie coefficients α_i, $1 \leqslant i \leqslant 6$ represent the anisotropic viscosities of the liquid crystal. In particular, α_4 corresponds to the isotropic or Newtonian viscosity. The parameter a in (7) quantifies the activity of the system, with $a = 0$ corresponding to the standard Ericksen-Leslie system for passive liquid crystals.

The active part (7) of the stress tensor accounts for the nonconservative forces generated by the individual fibers and are assumed to be dipolar. Their expressions were obtained from the symmetry of the flow field that they generate, with $a > 0$ corresponding to the extensile regime, and $a < 0$ to the contractile one [6–9] as illustrated in Fig. 1. In the terminology of *swimmers*, extensile particles are known as *pushers* and contractile ones as *pullers*.

The Leslie coefficients and the dissipativeness of the system: The rate of dissipation function, quadratic on the time-rate quantities, takes the form

$$\Delta = \tfrac{1}{2}[\alpha_1(\boldsymbol{n}^T\mathbf{A}\boldsymbol{n})^2 + \gamma_1|\mathbf{N}|^2 + (\alpha_5 + \alpha_6)|\mathbf{A}\boldsymbol{n}|^2 + (\alpha_3 + \alpha_2 + \gamma_2)\mathbf{N}^T\mathbf{A}\boldsymbol{n} + \alpha_4|\mathbf{A}|^2]. \tag{8}$$

The second law of thermodynamics in the form of the Clausius-Duhem inequality reduces to the positivity of the rate of dissipation function, $\Delta \geqslant 0$. Necessary and sufficient conditions for the latter result in the well-known inequalities [2]:

$$\alpha_1 + \tfrac{3}{2}\alpha_4 + \alpha_5 + \alpha_6 > 0, \quad 2\alpha_4 + \alpha_5 + \alpha_6 - \tfrac{\gamma_2^2}{\gamma_1} > 0, \quad \alpha_4 > 0, \quad \gamma_1 := \alpha_3 - \alpha_2 > 0, \quad \gamma_2 := \alpha_6 - \alpha_5. \tag{9}$$

Parodi's relation, a consequence of Onsager's reciprocal relations in the microscale description of liquid crystals, is an additional assumption of the theory:

$$\alpha_6 - \alpha_5 = \alpha_2 + \alpha_3. \tag{10}$$

This condition renders the rate of dissipation function of a potential for the viscous stress, that is, $\hat{\sigma} = \frac{\partial\Delta}{\partial\nabla\boldsymbol{v}}$. We consider a class of liquid crystals able to align under the effect of flow of small velocity gradient. This requires that

$$\left|\frac{\gamma_1}{\gamma_2}\right| := \frac{1}{\lambda} \leqslant 1, \tag{11}$$

λ known as the flow alignment parameter. It represents the ratio between the extensional and rotational effects of the shear flow, with the former dominating in the case $\lambda > 1$, and so the director aligns along the flow direction. The tumbling regime corresponds to $\lambda < 1$, with a prevailing rotational couple that prevents $\boldsymbol{n}$ from choosing an aligning direction [6,29]. Moreover

$$\gamma_2 < 0 \text{ (for rodlike)} \quad \text{and} \quad \gamma_2 > 0 \text{ (for disklike)} \tag{12}$$

nematics, respectively.

Boundary conditions: The behavior of active liquid crystals on the domain boundary may be significantly different from that of their passive counterparts. Whereas actin fibers may anchor and stick to the boundary, some active liquid crystals, such as microtubules, do not align by anchoring on the boundary and can only become oriented by flow. There is no evidence of nonslip behavior in experiments where microtubules are found to slide along the walls. Guided by experiments, slip-free boundary conditions were used in numerical simulations in [4]. Hence, we require

$$\boldsymbol{v} \cdot \boldsymbol{\nu} = 0, \quad (\sigma\boldsymbol{\nu}) \cdot \boldsymbol{\tau} = 0, \quad \text{on } \partial\Omega, \tag{13}$$

where $\boldsymbol{\nu}$ and $\boldsymbol{\tau}$ denote the outer unit normal and tangent vectors to the boundary, respectively. For the director field, we impose

zero Neumann boundary conditions:

$$\frac{d\boldsymbol{n}}{d\boldsymbol{\nu}} = 0 \text{ on } \partial\Omega. \tag{14}$$

When Ω is a semi-infinite stripe domain with thickness $2L_3$, suppose that the flow and director field are restricted to the xz-plane, and denote by ϕ the angle between $\boldsymbol{n}$ and the z-axis. Then, the conditions (13) and (14), respectively, become

$$v_3(x, -L_3) = v_3(x, L_3) = 0, \quad \sigma_{13} = 0, \tag{15}$$

$$\frac{d\phi}{d\boldsymbol{\nu}} = 0. \tag{16}$$

Remark: In the calculations for the stability analysis of both types of fibers, we impose Dirichlet boundary conditions on the perturbation angle rather than the Neumann condition (16). This has been done to simplify the stability analysis, but one would naturally expect different results for other boundary conditions.

A. Scaling and nondimensionalization

Next, we formulate the governing equations in terms of dimensionless time and space variables. For this, we choose the positive quantities L_1 and L_3 to be the characteristic lengths along the x and z directions, respectively, and let $V > 0$ denote the characteristic velocity. Moreover, we take the isotropic coefficient α_4 to be the characteristic viscosity of the system and let $p_0 > 0$ represent the typical pressure. The resulting dimensionless variables are

$$\tilde{x} = \frac{x}{L_1},\ \tilde{z} = \frac{z}{L_3},\ \tilde{v}_1 = \frac{v_1}{V},\ \tilde{v}_3 = \frac{v_3}{V},\quad \tilde{t} = \frac{t}{T},\ T = \frac{L_1}{V},$$

$$\bar{p} = \frac{p}{p_0},\ p_0 = \frac{V\eta}{L_1},\ \ell = \frac{L_3}{L_1}\text{: dimensionless width.}$$

The quantity $T > 0$ represents the typical timescale. We subsequently divide the governing equations, term by term, by the expression $\alpha_4 \frac{V}{L_1^2}$. The resulting equations involve well-known dimensionless parameter groups: the Reynolds number Re, the Ericksen number $\mathcal{E}_r$, and the activity parameter $\mathcal{A}$, as well as the aspect ratio of the channel, ℓ. The quantity $\mathcal{E}_r$ represents the ratio of the viscous to the elastic torques. Further, we multiply the equation of balance of angular momentum by $\frac{L_1^2}{k_1^2}$, which also brings $\mathcal{E}_r$ into the expression.

We also need the following nondimensional parameters:

$$\tilde{\alpha}_i = \frac{\alpha_i}{\rho V L_1}, \quad \tilde{\gamma}_i = \frac{\gamma_i}{\rho V L_1}, \quad \tilde{k} = \frac{k}{\rho V^2 L_1^2}, \tag{17}$$

where $\tilde{\alpha}_i$ and $\tilde{\gamma}_i$ are the dimensionless viscosity coefficients and $\tilde{k}$ is the dimensionless elastic modulus. The list of the dimensionless parameters groups of the model is

$$\mathcal{R}_e = \frac{L_1 V \rho}{\eta}\text{: Reynolds number,}$$

$$\mathcal{E}_r = \frac{\eta L_1 V}{k}\text{: Ericksen number,}$$

$$\mathcal{A} = \frac{aL_1}{V\eta}\text{: Activity number,} \tag{18}$$

where $\eta := \alpha_4$. In summary, the list of the model parameters is

$$\mathcal{P}_{EL} := \{\mathcal{R}_e, \mathcal{E}_r, \mathcal{A}, \ell, \alpha_i, \gamma_i\}. \tag{19}$$

Likewise, $\{\tilde{v}, \boldsymbol{n}, \tilde{p}\}$ and the Lagrange multiplier λ, maintaining the unit director constraint, are the unknown fields of the Ericksen-Leslie model. Since our work deals with the active liquid crystal confined in a channel, in a later section we will recast the governing equations in terms of two spatial dimensions.

B. Ericksen equations

In the theory of liquid crystals with variable degree of orientation [17], in addition to the director field $\boldsymbol{n}$ that describes the average direction of a molecular alignment, there is a scalar field $s \in (-\frac{1}{2}, 1)$ that describes the quality of the alignment. The value $s = 1$ corresponds to perfect alignment, $s = 0$ to the isotropic state, with $s = -\frac{1}{2}$ representing a state where the molecules are placed on a plane perpendicular to the director. For well aligned liquid crystals values of the variable s are between 0.5 and 0.8.

The role of the variable s can be understood in terms of the symmetric, traceless order tensor Q, the main variable in the Landau–de Gennes model ([24], chapter 3).

The uniaxial state of a liquid crystal corresponds to the case when two of the eigenvalues of Q are equal and different from the third one, with Q admitting the representation

$$Q = s\big(\boldsymbol{n} \otimes \boldsymbol{n} - \tfrac{1}{3}I\big). \tag{20}$$

Here $\boldsymbol{n}$ represents the eigenvector associated with the distinct eigenvalue s, the former being the director of the Oseen-Frank energy. Equilibrium states of the liquid crystal minimize the Landau–de Gennes energy [30], whose density is of the form

$$F_{\text{dGL}} = \mathcal{W}_{\text{LdG}}(Q, \nabla Q) + w(Q), \tag{21}$$

where $\mathcal{W}_{\text{LdG}}$ is a quadratic expression in terms of the third-order tensor ∇Q and w is a double-well potential that encodes the phase transition between the nematic and isotropic states. For special choices of the constants in $\mathcal{W}_{\text{LdG}}$ and restricting (21) to the uniaxial class (20), the energy becomes

$$F = s^2 W_{\text{OF}}(\boldsymbol{n}, \nabla \boldsymbol{n}) + k_0 |\nabla s|^2 + \nu w(s), \tag{22}$$

with $|\boldsymbol{n}| = 1$ and $s \in (-\frac{1}{2}, 1)$, and ν and k_0 positive constants. The scalar potential $w(s)$ is monotonically increasing as $s \to 1^+, -\frac{1}{2}^-$, expressing that it requires increasingly high energy to approach the ideal limiting states. Moreover, in the case of rodlike materials, there exists $0 < s^* < 1$ such that

$$w'(s^*) = 0,\ w''(s^*) \geqslant 0. \tag{23}$$

In standard liquid crystals s^* depends on the temperature and/or concentration. For dislike liquid crystals, the minimum, still designated by s^*, falls in the negative order parameter range. Figure 2 shows the scalar potential function $w(s)$ in the energy (22).

The governing system for the Ericksen model consists of the suitably modified equations (1)–(3) together with the generalized balance of angular momentum:

$$\beta_2(s)\dot{s} = \nabla \cdot \left(\frac{\partial F}{\partial \nabla s}\right) - \frac{\partial F}{\partial s} - \beta_3(s)\mathbf{n} \cdot \mathbf{An}. \tag{24}$$

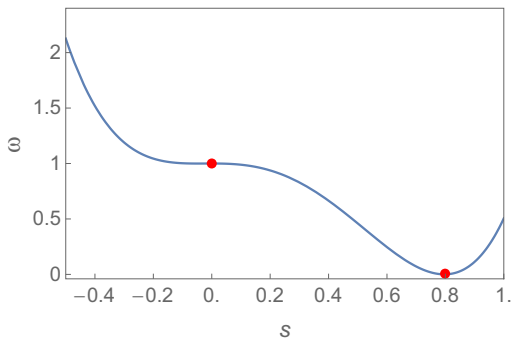

FIG. 2. Scalar potential function $w(s)$ corresponding to a rod-like nematic regime. The analogous potential for a discotic nematic would have its minimum at a negative value of s.

The modifications on the Ericksen-Leslie model involve the following:

(1) In the total energy, replace the Oseen-Frank form $W_{\rm OF}$ in (4) with Ericksen's energy F in (22).

(2) The Leslie coefficients α_i are now functions that depend on s and still satisfying the inequalities (9) and relations (10) and (11).

(3) The tensorial term $\beta_1(s)\dot{s}\,\boldsymbol{n}\otimes\boldsymbol{n}$, β_1 a scalar function, is now added to the viscous stress (6). Likewise, the term $k_0\nabla s\otimes\frac{\partial F}{\partial\nabla s}$ is included in the total stress (5) as a new elastic contribution.

(4) The active stress term (7) is now modified to $as^2\boldsymbol{n}\otimes\boldsymbol{n}$.

(5) The new viscosity coefficients satisfy $\beta_1=\beta_3<0$ and $\beta_2>0$, and the dimensionless parameter $\bar{\nu}=\nu\frac{L_1^2}{k}$ is added to the list (18).

The collection of parameters of the problem now becomes $\mathcal{P}:=\{\mathcal{R}_e,\mathcal{E}_r,\mathcal{A},\ell,\bar{\nu},\alpha_i,\gamma_i,\beta_i\}$.

III. THE MODEL

The proposed model directly emerges from the background Ericksen-Leslie equations when the shear flow geometry is assumed. Although such a geometry has received significant attention, the outcomes of dependence of the director orientation resulting from the combination of an active ingredient in confinement is less known. We will also explore conditions under which the basic flow develops a pattern. We suppress the superimposed bar notation and assume that all the variables are already dimensionless. We look for solutions such that the velocity field is unidirectional $\mathbf{v}=(U(z,t),0,0)$ and the director angle $\phi=\phi(z,t)$. From Eqs. (A1)–(A3) [18] we get, the reduced one-dimensional problem

$$\mathcal{R}_e\frac{\partial U}{\partial t}=-\frac{\partial p}{\partial x}+\ell^{-2}\frac{\partial}{\partial z}\left[g(\phi)\frac{\partial U}{\partial z}-\frac{\mathcal{A}\ell}{2}\sin 2\phi\right], \tag{25}$$

$$0=-\frac{\partial p}{\partial z}-2\mathcal{E}_r^{-1}\ell^{-3}\frac{\partial}{\partial z}\left[\left(\frac{\partial\phi}{\partial z}\right)^2\right]+\ell^{-2}\frac{\partial}{\partial z}\left[g_0(\phi)\frac{\partial U}{\partial z}-\mathcal{A}\ell\cos^2\phi\right], \tag{26}$$

$$-\frac{\gamma_1\ell^2}{2\alpha_4}\frac{\partial\phi}{\partial t}=\frac{\partial^2\phi}{\partial z^2}+\frac{\mathcal{E}_r\ell}{4\alpha_4}\frac{\partial U}{\partial z}(-\gamma_1+\gamma_2\cos 2\phi), \tag{27}$$

where

$$g(\phi)=\frac{1}{4\alpha_4}[\alpha_1\sin^2 2\phi+2(\alpha_5-\alpha_2)\cos^2\phi+2(\alpha_6-\alpha_3)\sin^2\phi+2\alpha_4], \tag{28}$$

$$g_0(\phi)=\frac{1}{4\alpha_4}[\alpha_4+2\alpha_1\sin 2\phi\cos^2\phi+(\alpha_2+\alpha_3+\alpha_5+\alpha_6)\sin 2\phi]. \tag{29}$$

The function $g(\phi)$ is the dimensionless form of the rate of dissipation Δ of the flow:

$$g(\phi)=\alpha_4^{-1}\Delta>0. \tag{30}$$

Next, we eliminate the pressure p from the equations of balance of linear momentum. Taking the partial derivative of Eq. (26) with respect to x, we get

$$0=\frac{\partial^2 p}{\partial z\partial x}. \tag{31}$$

Likewise, taking the derivative with respect to z in Eq. (25) and applying to it the previous result, we get

$$\mathcal{R}_e\frac{\partial^2 U}{\partial z\partial t}=\ell^{-2}\frac{\partial^2}{\partial z^2}\left[g(\phi)\frac{\partial U}{\partial z}-\frac{1}{2}\mathcal{A}\ell\sin 2\phi\right]. \tag{32}$$

Integrating once with respect to z, we get

$$\mathcal{R}_e\frac{\partial U}{\partial t}=\ell^{-2}\frac{\partial}{\partial z}\left[g(\phi)\frac{\partial U}{\partial z}-\frac{1}{2}\mathcal{A}\ell\sin 2\phi\right]+c_1(t), \tag{33}$$

where $c_1(t)$ is arbitrary. The governing system reduces now to Eqs. (27) and (33). Subsequent use of Eq. (26) determines the pressure.

1. *Steady state flow with constant angle of alignment*

Let us now look for one-dimensional fields $(U(z),0,0)$, $\phi=\phi(z)$, and $s=s(z)$. They satisfy the system of equations

$$0=g(\phi)\frac{dU}{dz}-\frac{1}{2}\mathcal{A}\ell\sin 2\phi+c_1 z+c_2, \tag{34}$$

$$0=\frac{d}{dz}\left(s^2\frac{d\phi}{dz}\right)+\frac{\mathcal{E}_r\ell}{4\alpha_4}\frac{dU}{dz}(-\gamma_1+\gamma_2\cos 2\phi), \tag{35}$$

where c_1 and c_2 are arbitrary constants obtained in setting $U_t\equiv 0$ in Eq. (33) and further integrating it with respect to z. Let us now determine the constants c_1 and c_2. We point out that combining Eq. (25) in the steady-state case with Eq. (34) yields

$$c_1=-\ell^2\frac{\partial p}{\partial x}.$$

We shall take $c_1=0$, which corresponds to the assumption that there is no applied external pressure gradient driving the flow. Furthermore, requiring that the velocity gradient vanishes when the activity is equal to zero implies that $c_2=0$. The resulting expression of the velocity gradient is then

$$U'(z)=\mathcal{A}\ell\sin(2\phi)/g(\phi), \tag{36}$$

Substitution of this equation into (35) gives

$$0=\frac{d}{dz}\left(s^2\frac{d\phi}{dz}\right)+\frac{\mathcal{E}_r\mathcal{A}\ell^2}{4\alpha_4 g(\phi)}\sin 2\phi(-\gamma_1+\gamma_2\cos 2\phi). \tag{37}$$

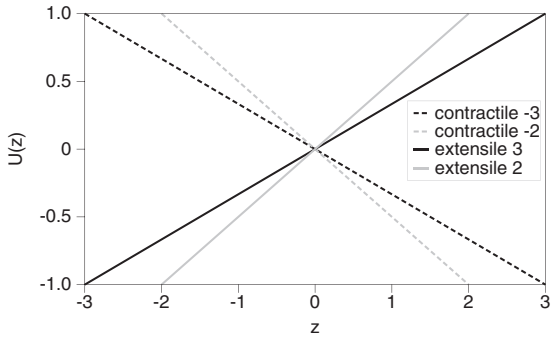

FIG. 3. Shear flow velocity profiles with shear rate $\mathcal{A}\ell \sin(2\phi)/g(\phi) = \pm 2$ (gray), ± 3 (solid black). Lines of positive rate correspond to the extensile regime and the negative correspond to contractile.

Next, we look for solutions of Eq. (37) such that ϕ and consequently $U'(z)$ are constant. The latter corresponds to the observed states with the linear velocity profile. The angle of orientation of the director is

$$\cos(2\phi) = \frac{\gamma_1}{\gamma_2}. \tag{38}$$

From the properties of γ_1 and γ_2 (12) for rodlike nematics, we observe that $\cos 2\phi < 0$ and so

$$\frac{\pi}{4} < \phi < \frac{\pi}{2}.$$

That is, the angle $0 \leqslant \frac{\pi}{2} - \phi \leqslant \frac{\pi}{4}$ between the director field and the horizontal direction is smaller than $\frac{\pi}{4}$ radians. Likewise, for dislike nematics (12), $\cos 2\phi > 0$ so

$$0 < \phi < \frac{\pi}{4},$$

and $\frac{\pi}{2} > \frac{\pi}{2} - \phi > \frac{\pi}{4}$. In either case, let us denote

$$\phi_0 = \frac{1}{2}\cos^{-1}\left(\frac{\gamma_1}{\gamma_2}\right). \tag{39}$$

The velocity field is given by

$$U(z) = \frac{\mathcal{A}\ell}{g(\phi)}\sin(2\phi)z, \tag{40}$$

where the constant of integration has been chosen to give the odd profile. We observe that the solutions show very good agreement with the experimental results. Indeed, in the shear flow regimes, the activity parameter does not directly influence the flow alignment, but it does increase the velocity gradient, i.e., the shear rate. (See Fig. 3).

Note that Eq. (38) shows that the director angle does not depend on the activity parameter $\mathcal{A}$ whose dependence enters the expression (40) of the velocity gradient. Both properties are found to be in a full agreement with experiments.

In order to derive alignment features of the constant flow solution, we need to appeal to the order parameter equation of Ericksen's system. In the current geometry, it is represented by Eqs. (40) and (38) and the solution of the scalar equation,

$$\bar{\nu} w'(s) = -\frac{\beta_3}{2\Delta}\mathcal{E}_r \mathcal{A}\ell^2 \sin^2 2\phi. \tag{41}$$

Since $\beta_3 < 0$ and $w'(s) > 0$, for $s^* > s > 1$, we conclude that Eq. (41) has a unique stable solution in the given interval, with its value increasing as either $\mathcal{A}$ or $\mathcal{E}_r$ increase [31]. This points to the analogous role of the *activity* $\mathcal{A}$ in active flows to that of the applied pressure gradient in passive Poiseuille flow. As for the passive flow, the loss of stability of the constant angle state may prevent the increase in order otherwise predicted by Eq. (41).

2. Steady-state flow with variable angle of alignment

Nonconstants solutions of Eqs. (37) and (36) represent a shear flow with variable director angle. In fact, the former corresponds to a nonlinear pendulum model, with two forcing terms, the active couple shown in (5) together with the torque inherent to shear flow, also encountered in passive systems.

IV. METHODS

A. Stability analysis framework

Henceforth, we study the stability of the solution $(U(z), \phi_0)$ under perturbations of the form

$$\tilde{v}_1 = U + \epsilon v_1(t, x, z),$$
$$\tilde{v}_3 = \epsilon v_3(t, x, z),$$
$$\tilde{\phi} = \phi_0 + \epsilon \phi_1(t, x, z),$$

where U in (40) and ϕ_0 in (39) are the shear base flow solution and s_0 and ϕ_0 are constant. Substituting these expressions into the full two-dimensional system of governing Eqs. (A1), (A2) and (A3) [18] we obtain the linear system (B1), (B2), and (B3) for the fields $(v_1(t, x, z), v_3(t, x, z), \phi_1(t, x, z))$.

Moreover, we propose the following exponential expressions of the unknown fields, consistent with those used in the normal mode stability analysis:

$$\Psi(t, x, z) = \psi(z)e^{i\omega(x-ct)}, \tag{42}$$

$$v_1(t, x, z) = \frac{\partial \Psi}{\partial z} = e^{i\omega(x-ct)}\frac{d\psi}{dz}, \tag{43}$$

$$v_3(t, x, z) = -\frac{\partial \Psi}{\partial x} = -i\omega\psi(z)e^{i\omega(x-ct)}, \tag{44}$$

where Ψ denotes the stream function of the flow. Also, for the direction angle, we assume that

$$\phi_1(t, x, z) = \Phi(z)e^{i\omega(x-ct)}. \tag{45}$$

Here ω and c are dimensionless complex numbers corresponding to the wave number and to the speed or growth of the perturbation, respectively. Specifically, separating Ψ and Φ into their real and imaginary parts, it follows that $\mathrm{Re}(\omega)$ represents the spatial oscillatory part of the perturbation and $\mathrm{Im}(c)$ corresponds to its time growth rate. From now on, we will restrict ourselves to the case when

$$\mathrm{Im}(\omega) = 0.$$

Substituting the expressions (42)–(45) into the linear governing Eqs. (B1), (B2) and (B3) [18], we obtain a linear system (C3) and (C4) [18] for the new variables. Specifically the former is a fourth-order linear ordinary differential equation for ψ and the latter is a second-order equation for Φ.

A relevant quantity in the analysis of flow which also helps quantify the transition to turbulence is the vorticity vector: $\boldsymbol{W} = \boldsymbol{\nabla} \times \boldsymbol{v}$. Since we are dealing with two-dimensional flow, it reduces to a scalar,

$$W(x,z) = \frac{\partial v_1}{\partial z} - \frac{\partial v_3}{\partial x} = e^{i\omega(x-ct)}\left[\frac{d^2\psi}{dz^2} - \omega^2\psi(z)\right]. \quad (46)$$

The governing equations for the perturbations are given by (C3) and (C4) in the Supplemental Materials [18], where their derivation is carried out.

We choose boundary conditions so that the boundary values of the base flow are not altered. The zero boundary conditions on perturbations suggest that a discretization using Chebyshev polynomials is appropriate. We apply the Chebyshev-QZ algorithm to solve the generalized eigenvalue problem resulting from the linearization of the governing system about the base shear flow. We emphasize the secondary role of the director field boundary conditions. Indeed, one important difference between active and passive liquid crystals is that whereas the latter can be aligned by surface anchoring, this is not the case for active flows, known to respond to alignment by flow only. Hence the requirement that the perturbations do not change the boundary values of the velocity and alignment of the basic solutions leads to imposing the conditions

$$\psi(\pm 1) = 0, \quad \psi'(\pm 1) = 0, \quad \Phi(\pm 1) = 0. \quad (47)$$

The numerical method

The Chebyshev polynomials [32,33] in the variable z form an orthogonal family on z-interval $[-1, 1]$. We apply the Chebyshev-QZ algorithm [34,35] to solve the generalized eigenvalue problem (47), (C3), and (C4).

We first approximate the stream function $\psi(z)$ and angle function $\Phi(z)$ by the truncated Chebyshev expansions

$$\psi(z) = \sum_{n=0}^{N} a_n T_n(z), \quad \Phi(z) = \sum_{n=0}^{N-2} b_n T_n(z), \quad (48)$$

where $T_n(z)$ denotes the nth-order Chebyshev polynomial of the first-kind. Our goal is to determine the coefficients a_n, b_n and the eigenvalue c. To keep the unknown coefficients evenly distributed over the two functions, we choose different orders of truncations for $\psi(z)$ and $\Phi(z)$.

We collocate the Galerkin truncation at the extrema of the Chebyshev polynomial

$$z = \cos\left(\frac{j\pi}{N-2}\right), j = 1, \ldots, N-3. \quad (49)$$

Thus, evaluating the governing equations at these extrema points, we obtain $2N - 6$ linear algebraic equations. Six additional relations are provided by the corresponding boundary conditions (47), which complete the system.

The substitution of the truncated expansions (48) into the boundary conditions yields rows of zeros, which produce a spurious eigenvalue [34], and therefore, we eliminate them. The full system of equations becomes the algebraic eigenvalue problem

$$[A_R + iA_I]\mathbf{x} = c[B_R + iB_I]\mathbf{x}, \quad (50)$$

where $\mathbf{x} = (a_3, \ldots, a_N, b_2, \ldots, b_{N-2})^T \in \mathbb{C}^{2N-5}$, A_R, A_I, B_R, and B_I denote $(2N-5)\times(2N-5)$ real matrices. Using the QZ algorithm of MATLAB, we obtain the eigenvalues and corresponding eigenvectors. Details of the steps leading to the system (50) are given by Eqs. (E1), (E2), and (E4) in the Supplemental Material [18]. We end this section by listing the values of the Leslie viscosity coefficients used in the simulations. For extensile liquid crystals, we take

$$\alpha_1 = 0,\ \alpha_2 = -1.5,\ \alpha_3 = -0.5,\ \alpha_4 = 2,$$
$$\alpha_5 = 2,\ \alpha_6 = 0,\ \gamma_1 = 1,\ \gamma_2 = -2. \quad (51)$$

The data list to be used in the simulations of contractile liquid crystals is

$$\alpha_1 = 0,\ \alpha_2 = -1.5,\ \alpha_3 = -0.5,\ \alpha_4 = 4,$$
$$\alpha_5 = -2,\ \alpha_6 = 0,\ \gamma_1 = 1,\ \gamma_2 = 2. \quad (52)$$

These provide simple values that still maintain the anisotropy of the viscosity, satisfy the positivity of the rate of dissipation function, and represent the aligning regime in each class. Moreover, we take the constant order parameter as $s_0 = 1.0$.

The numerical study yields plots of ω with respect to the $\mathcal{A}$, for different values of $\mathcal{E}_r$, ℓ, and $\mathcal{R}_e$, showing regions of the wave-number domain for which the corresponding perturbation is either stable or unstable, that is, whether it decays or grows in time. The study also yields plots of the streamlines, vorticity, and director angle of the perturbation fields. The tangent vector field of the former corresponds to the velocity field of the system. We focus on quantitatively understanding the role of the parameter values in determining the instability behavior. Specifically, we assume that the Leslie coefficients α_i are fixed and seek how the dimensionless parameters $\mathcal{E}_r$, $\mathcal{A}$, ℓ^2, and $\mathcal{R}_e$ affect the stability of the shear flow.

Our analysis follows along the lines of many previous investigations of the physical mechanisms that cause either instability or stability in terms of eigenmodes of the linearized system [36–38]. To characterize the stability of the shear flow steady state, we check the growth rate of the dominant unstable eigenmode of the perturbation that affects the system. For unstable systems, the largest value of the linear growth rate and the corresponding wave number excite the system and modify the basic state in some essential fashion. On the other hand, stable perturbation modes also modify the system but decay in time.

B. Flow with variable director angle

The approach to study such flows is based on classical results of the theory of nonlinear, boundary value problems for second-order ordinary differential equations. Specifically, the methods that we apply rely on the comparison of solutions of the governing equations with appropriately simplified forms and the Sturm-Liouville theory of oscillatory solutions of the latter. First, let us rewrite the equation as

$$\phi''(z) = \frac{m}{g(\phi)}\sin 2\phi\left(\cos 2\phi - \frac{\gamma_1}{\gamma_2}\right), \quad m := -\frac{\mathcal{E}_r\mathcal{A}\ell^2\gamma_2}{4\alpha_4}. \quad (53)$$

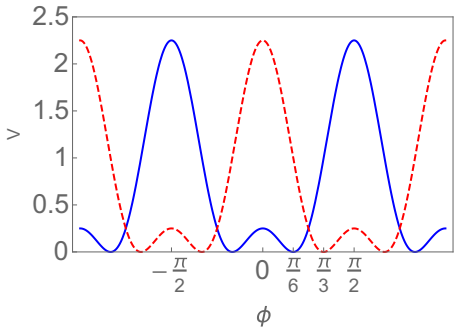

FIG. 4. Potential energy corresponding to Eq. (54), with $|\frac{\gamma_1}{\gamma_2}| = \frac{1}{2}$, for extensile (dashed line) and contractile fibers, respectively. The unstable rest states for each type of fiber correspond to $\phi = \frac{\pi}{2}, -\frac{\pi}{2}$. The stable stationary flows, with uniform director, correspond to $\phi = \frac{\pi}{3}, \frac{\pi}{6}$, for the extensile and compressible systems, respectively.

Note that $m > 0$ for both contractile and extensile fibers, since in both cases $\mathcal{A}\gamma_2 < 0$.

Theorem 1. Suppose that the viscosity coefficients satisfy the inequalities (9), (11), and (57), and satisfy $|\frac{\gamma_1}{\gamma_2}| < 1$. Then the rest states $\phi = \frac{\pi}{2}$ and $\phi = -\frac{\pi}{2}$, corresponding to horizontal alignment of the director field for extensile and contractile fibers, respectively, are unstable. Moreover, the uniformly aligned stationary states corresponding to Eqs. (39) and (40) are center equilibrium solutions. Furthermore, there exists $m_0 > 0$ such that bounded solutions of Eq. (53) exist and oscillate with a wave number $\sqrt{m_0}$ such that

$$M^- \geqslant m_0 \geqslant M^+,$$

with $M^\pm$ as in (59).

First, note that the conclusions on the instability of the equilibrium solutions $\phi = \pm\frac{\pi}{2}$ as well as on the stability of the uniformly aligned stationary states follow from standard phase plane analysis, which uses the auxiliary potential (55), shown in Fig. 4, as well as a calculation involving the specific form of $g^{-1}(\phi)$ in (53). The main part of the proof involves three steps.

1. Step 1

We first consider the following auxiliary equation:

$$\phi''(z) - M\sin 2\phi\left(-\frac{\gamma_1}{\gamma_2} + \cos 2\phi\right) = 0, \tag{54}$$

with $M > 0$ constant. It can also be written as $\phi''(z) + M\frac{\gamma_2}{\gamma_1}\sin 2\phi - \frac{M}{2}\sin 4\phi = 0$, which is the pendulum equation subject to two forces with different wave numbers. Multiplying Eq. (54) through by ϕ' and integrating it with respect to z once, we obtain the energy integral

$$\frac{1}{2}\phi'^2 + V(\phi) = E,\ V(\phi) = \frac{M}{2}\left(-\frac{\gamma_1}{\gamma_2} + \cos 2\phi\right)^2, \tag{55}$$

where $E \geqslant 0$ is an arbitrary constant. An example of the potential energy in (55) is shown in Fig. 4 [39,40].

A phase plane analysis of Eq. (54) shows the existence of periodic solutions with wave number of the order $\sqrt{M}$.

2. Step 2

Starting with the relation $\Delta = 4\alpha_4 g(\phi)$, which positivity is guaranteed by Leslie's inequalities (9), we express it as a quadratic polynomial of $\cos 2\phi$,

$$\Delta = -\alpha_1\cos^2 2\phi + (\alpha_5 + \alpha_3 - 2\alpha_6)\cos 2\phi + (\alpha_5 - \alpha_3 + 2\alpha_4 + \alpha_1). \tag{56}$$

Let us place additional assumptions on α_i, specifically,

$$m^- := \alpha_5 - \alpha_3 + 2\alpha_4 - |\alpha_2 + \alpha_6| > 0. \tag{57}$$

It can be easily verified that

$$m^+ := (\alpha_5 - \alpha_3 + 2\alpha_4 + \alpha_1) \geqslant \Delta \geqslant m^-. \tag{58}$$

Note that the coefficients in (51) and (52) satisfy the previous inequalities. This leads us to consider two differential equations of the type (54) with

$$M = M^+ := \frac{m}{m^+}, \quad M = M^- := \frac{m}{m^-}, \tag{59}$$

respectively.

3. Step 3

To show existence of periodic solutions of the original Eq. (53), we first consider two auxiliary equations of the form (54), with $M = M^{pm}$, as in (59), respectively. Applying the Sturm comparison theorem for second order ordinary differential equations [41] to each of the latter equations together with (53) allows us to conclude the existence of periodic solutions of Eq. (53).

V. RESULTS AND DISCUSSION

A. Stability analysis: Contractile fibers and comparison with the extensile

We study the plane shear flow of active liquid crystals in the aligning regime. We now present and discuss the results obtained by analyzing the governing equations and numerically solving the algebraic systems (50) corresponding to contractile systems $\mathcal{A} < 0$ to determine the normal instability threshold for different parameter values. We summarize the main results of the analysis and the ensuing graphs as follows.

We find solutions with linear velocity profiles and constant angles of alignment that agree with experimental observations of active filaments in a channel when $\mathcal{A} > 0$ [4]. We also find a velocity gradient of equal magnitude but opposite sign for the flow of contractile fibers. For both types of fibers, we find that the magnitude of the velocity gradient is proportional to the activity parameter, and the angle of alignment solely depends on the ratio of two relevant anisotropic viscosity coefficients, as in the case of a passive shear flow.

A prediction that emerges from the analysis of the order parameter is the increase in order as the activity number increases. In the case $\mathcal{A} > 0$, should the aligned shear flow remain stable, it would become highly ordered at a sufficiently large activity number. Likewise, for contractile fibers, increasing $|\mathcal{A}|$ tends to place the plank molecular groups on planes perpendicular to $\boldsymbol{n}$. Such conclusions follow from Eq. (41), together with the profile of the potential shown in Fig. 2 and the property of its critical points (23).

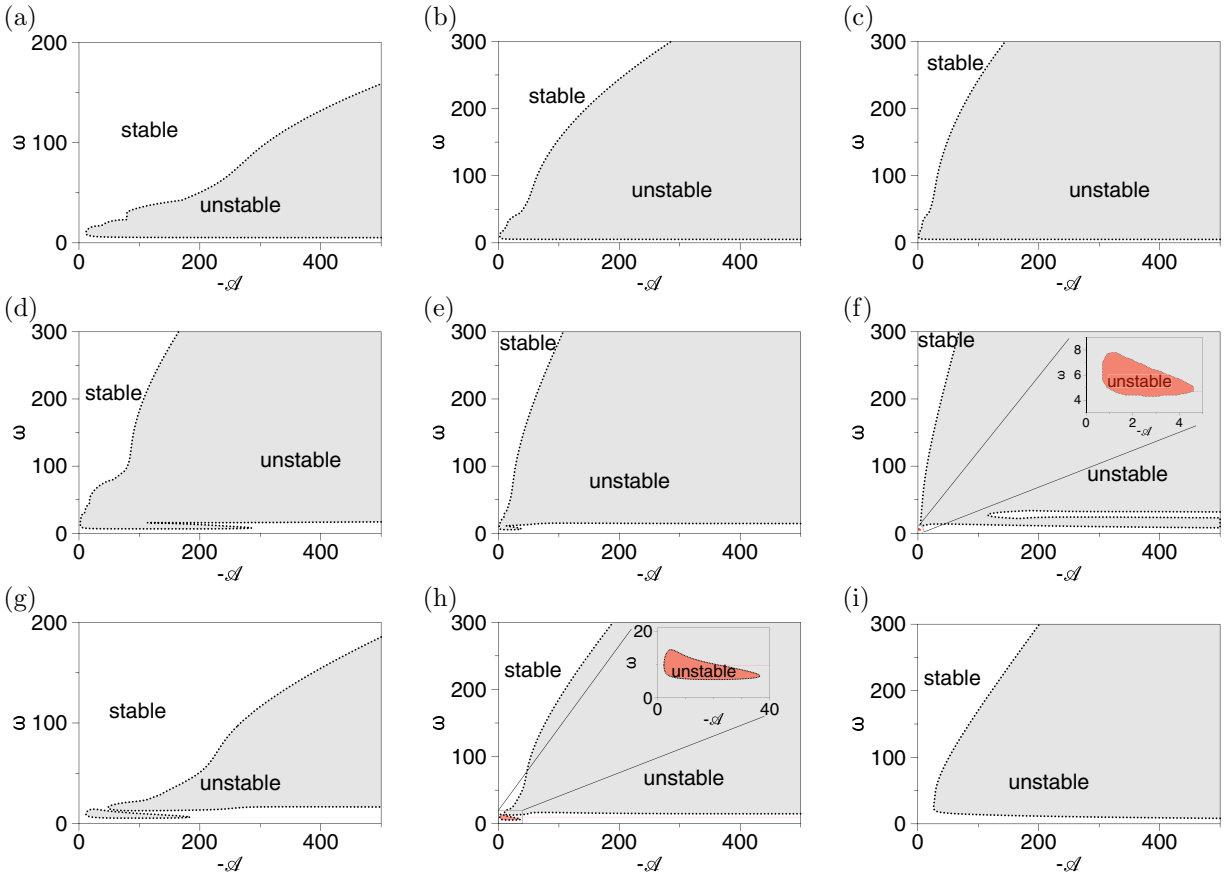

FIG. 5. Regions of stability in the $|\mathcal{A}|\omega$-plane. Plots (a)–(c) correspond to $\mathcal{R}_e = 0.1$ and $\ell = 0.2$ but different Ericksen numbers; plots (d)–(f) correspond to $\mathcal{E}_r = 1000$ and $\mathcal{R}_e = 5$, but different channel ratios ℓ; plot (g) is for small Ericksen number $\mathcal{E}_r = 100$, $\ell = 0.2$, and $\mathcal{R}_e = 1$; plot (h) is for medium $\mathcal{E}_r = 500$, $\ell = 0.2$, and $\mathcal{R}_e = 5$; and plot (i) is for $\mathcal{E}_r = 250$, $\ell = 0.4$, and $\mathcal{R}_e = 5$.

The increase of the interval of unstable wave numbers as $|\mathcal{A}|$ increases is an ongoing feature found in all the graphs in the $|\mathcal{A}|\omega$ plane, as in Figs. 5, 6(d), 6(e), and 7(a).

In all graphs, the range of accessible wave numbers is determined by two relevant length scales: the typical width of a fiber bundle (about 50 μm) and the length L_x of the experimental apparatus (giving the smallest accessible dimensionless wavelength of 1). We also recover the *essential instability* [9], that is, the fact that there is always a stable (flow) region near $\mathcal{A} = 0$ (due to the rest state becoming unstable). The $|\mathcal{A}|$-width of the latter shows dependency on $\mathcal{E}_r$ and l, as can be seen from Figs. 5(a)–5(c) and 5(d)–5(f), respectively, with the stable region narrowing as $\mathcal{E}_r$ and l increase. We also note that, for $\mathcal{E}_r = 1000$, such a region is nearly thinned out for wave numbers in the range 10–20, as the instability features of passive flow with large $\mathcal{E}_r$ emerge. We also note that, for all parameters of the flow, there is always a small wave length range where the flow is always stable. A recurrent property of the system is the increase of the area of the unstable region in the $|\mathcal{A}|\omega$-plane as, each, ℓ and $\mathcal{E}_r$ increase, while the other parameters remain fixed. Figures 5(a)–5(c) show the effect of increasing $\mathcal{E}_r$ from 10 to 1000 on the area of the regions. The analogous effect with increasing ℓ shown in Figs. 5(d)–5(f) is weaker.

Another relevant finding is the rich structure of the diagrams near their low left corner, that is, at the low wave-number regime with $|\mathcal{A}|$ small. This effect becomes accentuated with the increase of the $\mathcal{R}_e$ number. Although no specific experimental connection can be established at this point, we point out that such effects are ubiquitous in actin-type fibers subject to low-intensity stimulus, either active or passive [42,43]. It may be due to a plastic-type material rearrangement at the molecular scale, with the tendency to stretching of the filament due to shear being opposed by the natural contractile one, an effect also observed in some non-Newtonian fluids [44]. For instance, this type of behavior is also exhibited by the actin network in red blood cells and serves as a mechanism to support shear in small capillary domains [43]. However, in our case, we have not found sufficient experimental evidence to support such tentative conclusions.

The Reynolds number also significantly affects the instability patterns, especially for values above $\mathcal{R}_e = 1$. One feature is the presence of a low wave-number stability region across $|\mathcal{A}|$ [Figs. 5(d)–5(h), 7(a), and 6(e)]. However, the nucleation of an unstable region near the origin is also found, for $\mathcal{R}_e = 5$, $\mathcal{E}_r = 1000$, and $\ell = 0.4$ [Fig. 5(f)] and for $\mathcal{R}_e = 5$, $\mathcal{E}_r = 500$, and $\ell = 0.2$. For even higher $\mathcal{R}_e$-number, features emerge that are reminiscent of those found in the analysis of the Orr-Sommerfeld equation for shear flow of isotropic, Newtonian fluids [Fig. 6(e), for $\mathcal{R}_e = 100$, with the remarkable *whale head* profile at $\mathcal{E}_r = 500$].

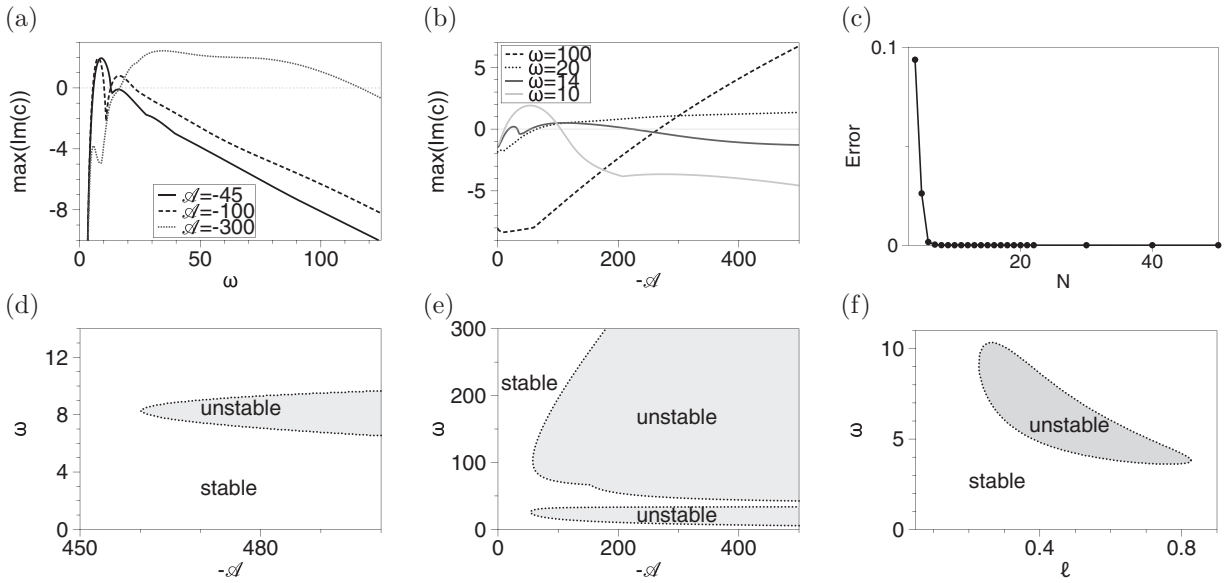

FIG. 6. (a, b) Growth rates, Im(c), at fixed activity number $\mathcal{A}$ and fixed ω for $\mathcal{R}_e = 1$, $\mathcal{E}_r = 100$, and $\ell = 0.2$. (c) The relative error of the computations with respect to the degree of the approximating polynomial in (48). (d, e) Regions of stability in the $|\mathcal{A}|\omega$-plane for the large Reynolds number regime ($\mathcal{R}_e = 100$) and fixed channel ratio $\ell = 0.2$: (d) for $\mathcal{E}_r = 5$ and (e) for $\mathcal{E}_r = 500$. (f) The region of stability in the $\ell\omega$-plane. This plot corresponds to $\mathcal{R}_e = 0.1$, $\mathcal{E}_r = 100$, and $\mathcal{A} = -10$.

Figures 6(a) and 6(b) show the detailed maximum growth rates max(Im(c)). They are corresponding to the horizontal and vertical sliding through the stability region shown in Fig. 5(g). Both graphs show a complex behavior at low frequencies [Fig. 6(a)] and for small values of $|\mathcal{A}|$ [Fig. 6(b)]. For $\omega = 100$, the growth rate increases linearly with respect to $|\mathcal{A}|$.

Figure 6(c) shows the relative error of the numerical approximations with respect to degree of the Chebyshev polynomial used in the simulation. Figure 6(f) plots the stability region in the $\ell\omega$-plane, as the active number $\mathcal{A} = -10$ is fixed.

The comparisons between the contractile fibers and the extensile fibers are shown in Fig. 7. Simulations for those figures are with different ranges of $\mathcal{A}$, but the same $\mathcal{R}_e = 1$, $\mathcal{E}_r = 1000$, and $\ell = 0.2$. The other parameters are in (51) and (52) for corresponding type fibers.

Figure 7(a) shows the stability region of the contractile fibers, and Fig. 7(b) shows the maximum growth rates in time as active number $\mathcal{A}$ is fixed. Each curve describes the detailed max(Im(c)) as we slide through the stability region 7(a) vertically. When we slide through the stability region horizontally, that will give a curve in Fig. 7(c). There are complicated growth rates when $\omega \in (0, 500)$. Figure 7(d) shows

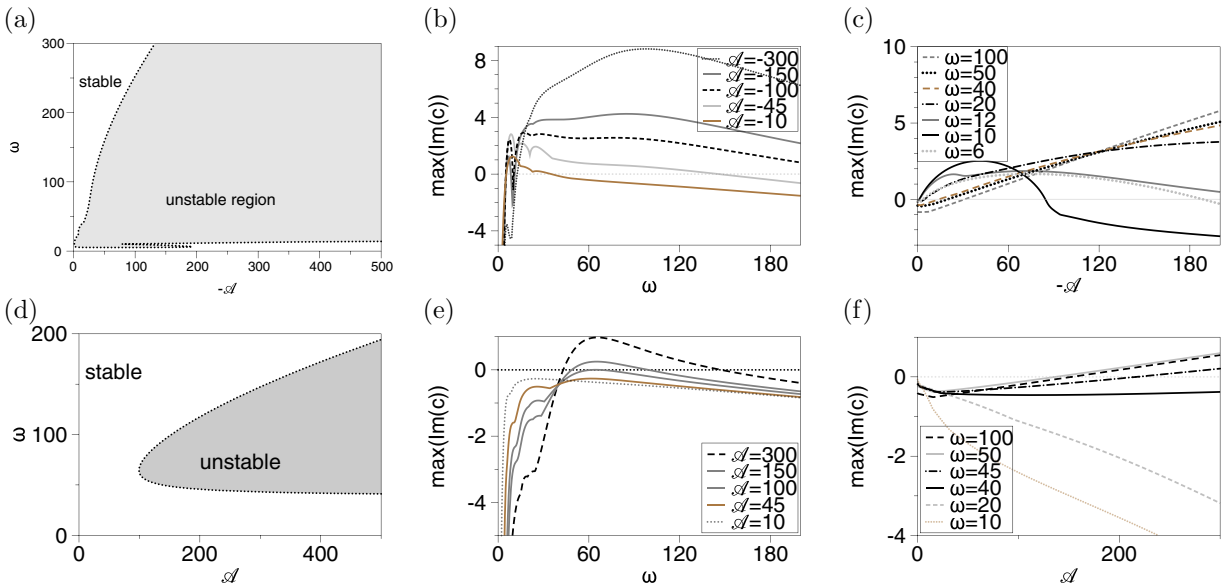

FIG. 7. The region of stability in the $\mathcal{A}\omega$-plane and growth rates with either activity number $\mathcal{A}$ fixed or perturbation wave number ω fixed. These plots correspond to $\mathcal{R}_e = 1$, $\mathcal{E}_r = 1000$, and $\ell = 0.2$.

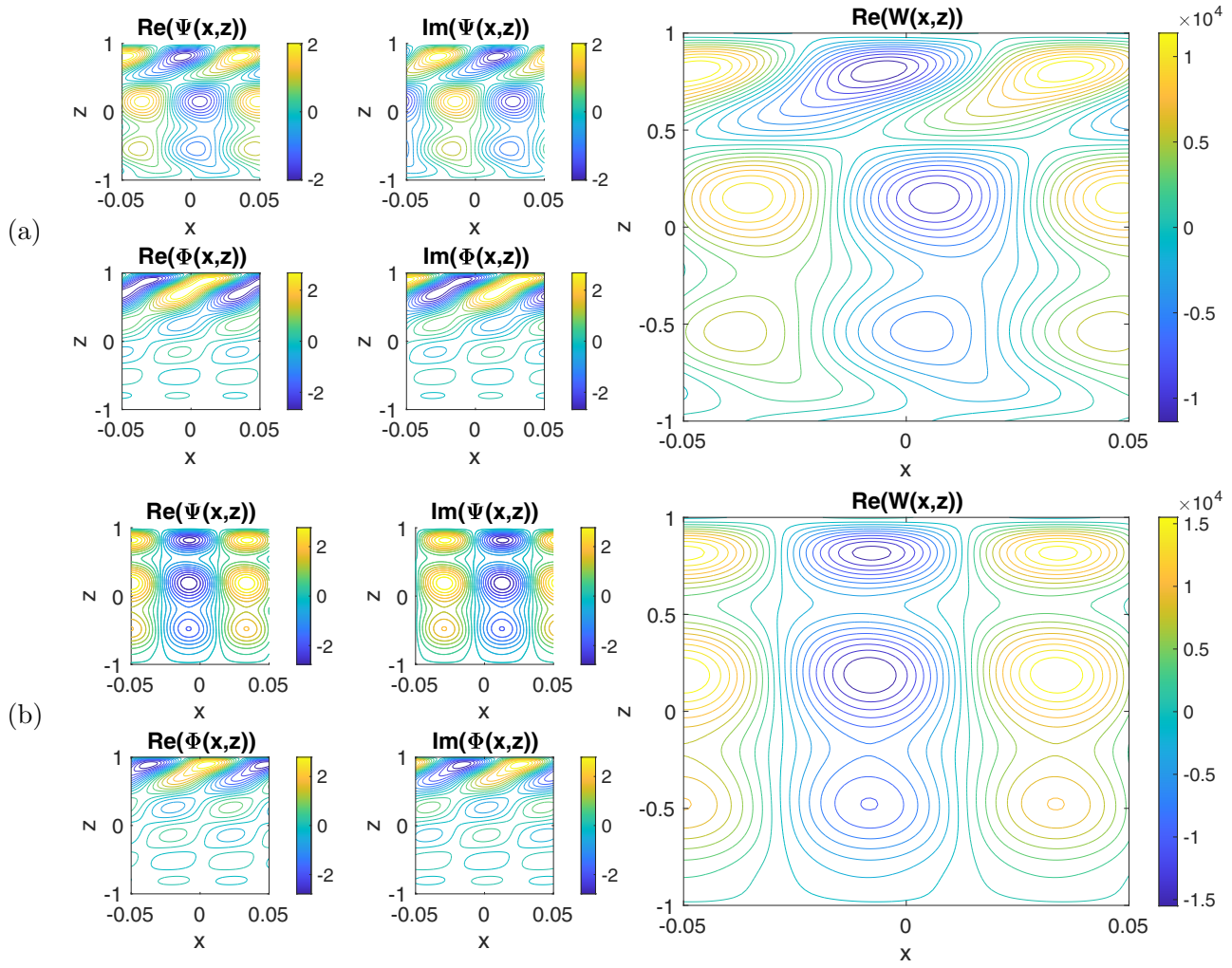

FIG. 8. Streamlines and the vorticity field for the perturbation modes with the largest eigenvalue. (a) $\mathcal{E}_r = 1000$, $\mathcal{R}_e = 5$, $\ell = 0.2$, $\omega = 75$, and $\mathcal{A} = -200$. (b) $\mathcal{E}_r = 1000$, $\mathcal{R}_e = 5$, $\ell = 0.2$, $\omega = 75$, and $\mathcal{A} = -10$.

the stability region of extensile fibers studied in our previous paper [3]. This is a direct comparison with the corresponding contractile fibers in Fig. 7(a). Figures 7(e) and 7(f) are detailed $\max(\mathrm{Im}(c))$ as we slide through the region in Fig. 7(d) horizontally and vertically. So far, the trend shows that the contractile stabilizes at lower frequencies than the extensile fiber case. Unstable growth rates change with more complicated behavior than those for extensile fibers. For example, with $\mathcal{A} = -100$, the system starts with a stable region. As ω increases, it enters an unstable region, then becomes stable for a narrow range of ω, reentering a large unstable region, to finally becoming stable for large ω. Even in the second unstable region, the maximum growth rate is not monotone increasing or decreasing. For the extensile fiber, when $\mathcal{A} = 100$ is fixed, the system also starts in a stable region (with monotonic growth rate), then enters the single unstable region, moving out of it near $\omega = 65$. Figures 8 and 9 illustrate modes of the fields that perturb the basic shear flow. Specifically, they include the profiles of the vorticity, streamlines, and director angle. One observation is the increase of the vorticity range as $\mathcal{A}$ increases, whether the perturbation is unstable [Figs. 8(a) and 9(a)] or stable [Figs. 8(b) and 9(b)]. In particular, we point out that the maximum vorticity in Fig. 8(b) (with $\mathcal{A} = -10$) is 600 dimensionless units, whereas the remaining figures (all of them with $\mathcal{A} = -200$) show the maximum range of 10^4 (according to the color coding). However, the parameters ℓ, $\mathcal{R}_e$, and $\mathcal{E}_r$ do not play the same role in changing the vorticity range of the perturbing flow. For instance, Fig. 8(a) (corresponding to $\mathcal{E}_r = 1000$) and Fig. 9(b) ($\mathcal{E}_r = 100$) show the same vorticity range of 10^4 dimensionless units. In both cases, $\mathcal{A} = -200$.

Figures 8(a) ($\mathcal{A} = -200$) and 8(b) ($\mathcal{A} = -10$) also indicate an increase of the range of values of the stream function with respect $\mathcal{A}$. Since the plots have a common geometrical domain, we can infer an increase of the magnitude of the velocity field itself. In Fig. 8(a) we estimate a distance of 0.25 dimensionless units along the z-direction between the center and the boundary of a vortex, with a change of 1.5 dimensionless units of the stream function. This gives $\frac{\partial \mathrm{Re}(\psi)}{\partial z} \approx \frac{1.25}{0.25} = 6$ as a velocity estimate. Likewise, we get $\frac{0.1}{0.25} = 0.4$ for the perturbing velocity field in Fig. 8(b).

B. Flow with variable director angle

One outcome of the analysis outlined in the Methods section is that the rest states $\phi = \frac{\pi}{2}$ and $\phi = -\frac{\pi}{2}$, corresponding to horizontal alignment of the director field for

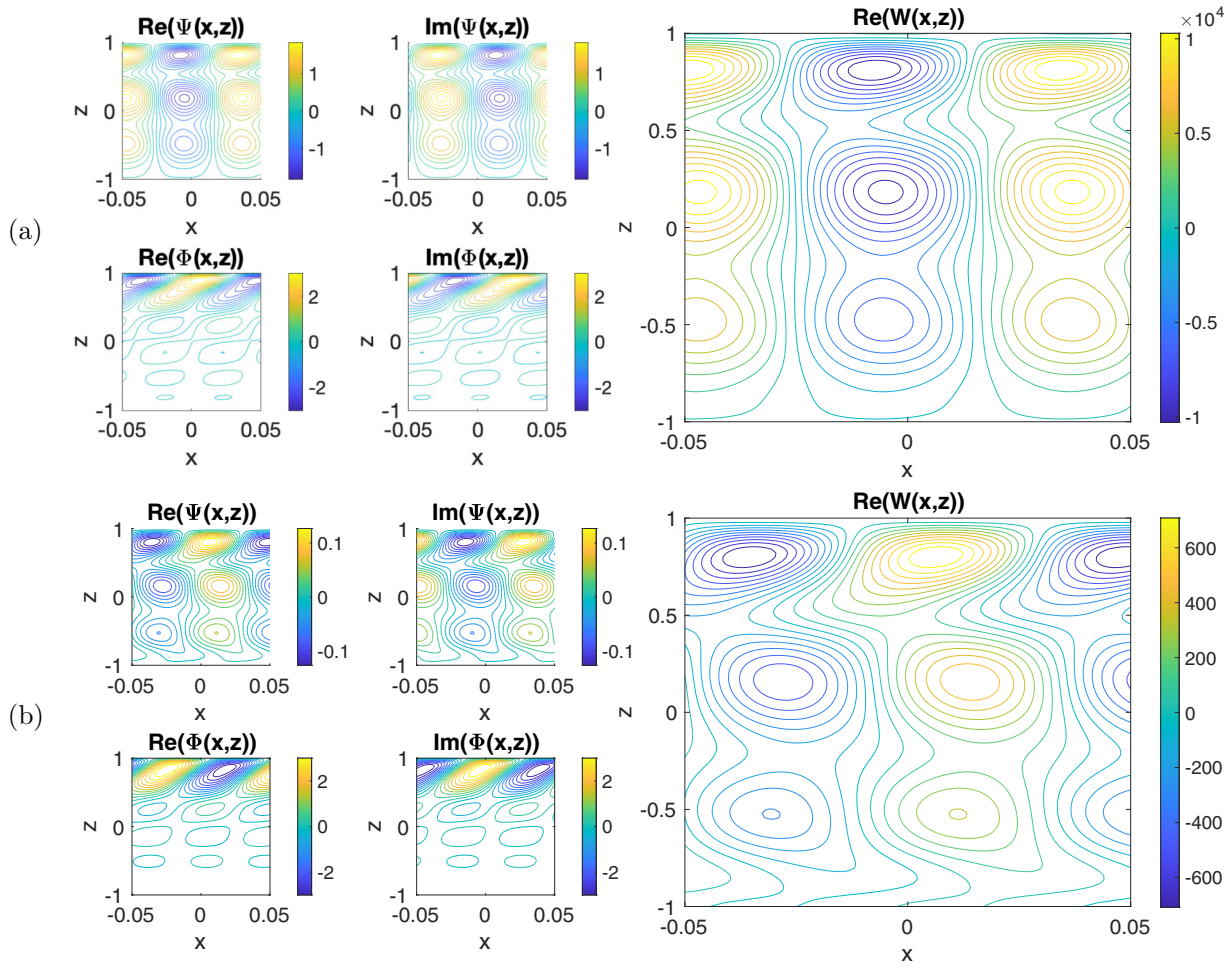

FIG. 9. Streamlines and the vorticity field for the perturbation modes with the largest eigenvalue. (a) $\omega = 75$, $\mathcal{R}_e = 0.1$, $\ell = 0.2$, $\mathcal{E}_r = 1000$, and $\mathcal{A} = -200$ and (b) $\omega = 75$, $\mathcal{R}_e = 5$, $\ell = 0.2$, $\mathcal{E}_r = 100$, and $\mathcal{A} = -200$.

extensile and contractile fibers, respectively, are unstable. We note that the perturbations are a subclass of the more general ones discussed in the previous subsection and have the same geometry as the solutions ($\phi = \phi(z), U = U(z)$). However, in both cases, the results confirm the *essential instability* of the rest state, a signature of active matter. The analysis also predicts the emergence of oscillatory states with wave number $\sqrt{m_0}$, where $m_0 > 0$ satisfies $M^- \geqslant m_0 \geqslant M^+$, with $M^\pm$ as in (57) and (59). In addition to the quantities $\mathcal{A}$, $\mathcal{E}_r$, the isotropic and rotational viscosities α_4 and γ_2, respectively, the rate of dissipation Δ plays a main role in determining the wave number of the oscillatory solutions. We note that the wave number m_0 increases with $\mathcal{E}_r$ and $\mathcal{A}$. In the estimate of the wave number, we used the inequalities (57) which are more restrictive than those in (9) but are satisfied by aligning liquid crystals such as MBBA and 5CB [15], and also by the viscosity data in used in the stability calculations of the current work. The predicted oscillations are are consistent with experimental observations of undulating pattern of confined extensile fibers at low activity [14].

VI. CONCLUSION

This article examines the onset of instability of a uniformly aligned shear flow of active matter in a confined channel, for both extensile and contractile fibers. The stability plots in the $\mathcal{A}\omega$-plane for extensile fibers indicate positive threshold value of $\mathcal{A}$ at which the system becomes unstable. This critical value decreases with increasing values of $\mathcal{E}_r$ and ℓ, and with the range of unstable frequencies also increasing. The growth rate profile calculated with respect to $\mathcal{A}$ shows a parabolic shape for low frequencies becoming linear at a threshold wave number. The profile of $\mathrm{Im}(c)$ with respect to ω starts being positive for all values of $\mathcal{A}$, reaching zero growth at a threshold value of ω that appears to be independent of $\mathcal{A}$. With further increase of ω, $\mathrm{Im}(c)$ reaches a positive maximum, subsequently tending to zero as ω increases, a feature that is also independent of $\mathcal{A}$. These trends have been reported in the experimental literature [4].

The stability plots in the $\mathcal{A}\omega$-plane for contractile fibers follow a pattern analogous to the extensile ones in that the range of unstable frequencies increases with $|\mathcal{A}|$, $\mathcal{E}_r$, and ℓ. However, there is no threshold value of $|\mathcal{A}|$ at which the unstable frequencies set in. Rather, the stability pattern for small $|\mathcal{A}|$, which is associated to small wave number values, is very complex, showing to be highly sensitive to the Reynolds number, which also affects other regions of the $\omega - \mathcal{A}$ diagram. This is a feature not shown by the extensile fibers. The plot of the growth rate $\mathrm{Im}(c)$ with respect to ω starts being

nonconvex at small ω and becomes decreasing. When plotted as a function of $|\mathcal{A}|$, it tends to a approach a wave-number-dependent constant value, showing an increasing profile for higher frequencies.

In future works, we will investigate the behavior of contractile fibers in the low-activity regime and its connection to plasticity, a signature of actin systems in the cell and the cytoplasm environment, being responsible for many physiological functions. For both types of fibers, the results point to a transition towards turbulent regimes as the width of the channel or the level of activity increase. The follow up work on extensile fibers will examine the observed pairwise, $(\pm\frac{1}{2})$ defect elimination that accompanies the transition to turbulence. To the authors' knowledge, experiments for active contractile fibers, at low-activity regimes and analogous to those involving extensile ones, are much scarcer. This may be due to the low-activity instability and plasticity behaviors of the contractile systems. From this point of view, the work presented here provides quantitative information on such regimes and may help bridge the gap between both such systems.

ACKNOWLEDGMENTS

M.C.C. gratefully acknowledges the support of the National Science Foundation through Grants No. DMS-1435372 and No. DMS-DMREF1729589. D.G. acknowledges funding from the National Science Foundation through Grant No. DMS-1729538. L.Y. acknowledges the support of the National Science Foundation Grant No. DMS 1852597.

[1] F. M. Leslie, Some thermal effects in cholesteric liquid crystals, Proc. R. Soc. London A **307**, 359 (1968).
[2] F. M. Leslie, Continuum theory for nematic liquid crystals, Continuum Mech. Thermodyn. **4**, 167 (1992).
[3] L. Zhao, L. Yao, D. Golovaty, J. Ignés-Mullol, F. Sagués, and M. C. Calderer, Stability analysis of flow of active extensile fibers in confined domains, Chaos **30**, 113105 (2020).
[4] J. Hardoüin, R. Hughes, A. Doostmohammadi, J. Laurent, T. Lopez-Leon, J. M. Yeomans, and J. Ignés-Mullol, and F. Sagués, Reconfigurable flows and defect landscape of confined active nematics, Commun. Phys. **2**, 121 (2019)..
[5] T. Sanchez, D. Chen, S. DeCamp, M. Heymann, and Z. Dogic, Spontaneous motion in hierarchically assembled active matter, Nature (London) **491**, 431 (2012).
[6] S. A. Edwards and J. M. Yeomans, Spontaneous flow states in active nematics: A unified picture, Europhys. Lett. **85**, 18008 (2009).
[7] M. C. Marchetti, J. F. Joanny, S. Ramaswamy, T. B. Liverpool, J. Prost, M. Rao, and R. Simha, Hydrodynamics of soft active matter, Rev. Mod. Phys. **85**, 1143 (2013).
[8] D. Marenduzzo, E. Orlandini, and J. M. Yeomans, Hydrodynamics and Rheology of Active Liquid Crystals: A Numerical Investigation, Phys. Rev. Lett. **98**, 118102 (2007).
[9] S. Ramaswamy, The mechanics and statistics of active matter, Annu. Rev. Condens. Matter Phys. **1**, 323 (2010).
[10] S. Ramaswamy and M. Rao, Active-filament hydrodynamics: Instabilities, boundary conditions and rheology, New J. Phys. **9**, 423 (2007).
[11] R. Voituriez, J. F. Joanny, and J. Prost, Spontaneous flow transition in active polar gels, Europhys. Lett. **70**, 404 (2005).
[12] G. Duclos, C. Blanch-Mercader, V. Yashunsky, G. Salbreux, J.-F. Joanny, J. Prost, and P. Silberzan, Spontaneous shear flow in confined cellular nematics, Nat. Phys. **14**, 728 (2018).
[13] M. L. Gardel, J. H. Shin, F. C. MacKintosh, L. Mahadevan, P. Matsudaira, and D. A. Weitz, Elastic behavior of cross-linked and bundled actin networks, Science **304**, 1301 (2004).
[14] P. Guillamat, J. Ignés-Mullol, and F. Sagués, Taming active turbulence with patterned soft interfaces, Nat. Commun. **8**, 564 (2017).
[15] R. G. Larson, *The Structure and Rheology of Complex Fluids*, Topics in Chemical Engineering Vol. 150 (Oxford University Press, New York, 1999).
[16] B. J. Edwards, A. N. Beris, and M. Grmela, Generalized constitutive equation for polymeric liquid crystals Part 1. Model formulation using the Hamiltonian (Poisson bracket) formulation, J. Non-Newtonian Fluid Mech. **35**, 51 (1990).
[17] J. Ericksen, Liquid crystals with variable degree of orientation, Arch. Ration. Mech. Anal. **113**, 97 (1991).
[18] See Supplemental Material at http://link.aps.org/supplemental/10.1103/PhysRevE.104.034607 for the explicit expressions of the governing equations (A), the shear flow equations (B) and the set up of the stability analysis (C).
[19] J. L. Ericksen, Inequalities in liquid crystal theory, Phys. Fluids **9**, 1205 (1966).
[20] J. Ericksen, Nilpotent energies in liquid crystal theory, Arch. Ration. Mech. Anal. **10**, 189 (1962).
[21] F. C. Frank, I. Liquid crystals. On the theory of liquid crystals, Discuss. Faraday Soc. **25**, 19 (1958).
[22] C. W. Oseen, The theory of liquid crystals, Trans. Faraday Soc. **29**, 883 (1933).
[23] H. Zocher, Über die optische Anisotropie selektiv absorbierender Stoffe und über mechanische Erzeugung von Anisotropie, Naturwissenschaften **13**, 1015 (1925).
[24] P. G. de Gennes and J. Prost, *The Physics of Liquid Crystals*, International Series of Monographs in Physics Vol. 83 (Oxford University Press, New York, 1993).
[25] A. N. Beris and B. J. Edwards, *Thermodynamics of Flowing Systems: With Internal Microstructure*, Oxford Engineering Science no. 36 (Oxford University Press on Demand, Oxford, 1994).
[26] M. C. Calderer and B. Mukherjee, Chevron patterns in liquid crystal flows, Phys. D: Nonlinear Phenomena **98**, 201 (1996)
[27] K. F. Wissbur, Rheology of rod-like polymers in the liquid crystals, J. Rheol. **25**, 619 (1981).
[28] J. Ericksen, Continuum theory of nematic liquid crystals, Res. Mechanica **21**, 381 (1987).
[29] D. Baalss and S. Hess, The viscosity coefficients of oriented nematic and nematic discotic liquid crystals, Z. Naturforsch. A **43**, 662 (1988).
[30] B. Davies, *Integral Transforms and Their Applications*, Mathematical Sciences, Vol. 25 (Springer-Verlag, Berlin, Heildelberg, New York, 1978).
[31] M. C. Calderer and B. Mukherjee, Some mathematical issues in the modeling of flow phenomena

of polymeric liquid crystals, J. Rheol. **42**, 1519 (1998).

[32] K. C. Toh and L. N. Trefethen, The Chebyshev polynomials of a matrix, SIAM J. Matrix Anal. Appl. **20**, 400 (1998).

[33] L. N. Trefethen, *Spectral Methods in MATLAB* (SIAM, New York, 2001).

[34] J. J. Dongarra, B. Straughan, and D. W. Walker, Chebyshev tau-QZ algorithm methods for calculating spectra of hydrodynamic stability problems, Appl. Num. Math. **22**, 399 (1996).

[35] D. Bourne, Hydrodynamic stability, the Chebyshev tau method and spurious eigenvalues, Continuum Mech. Thermodyn. **15**, 571 (2003).

[36] A. E. Fraser, P. W. Terry, E. G. Zweibel, and M. J. Pueschel, Coupling of damped and growing modes in unstable shear flow, Phys. Plasmas **24**, 6 (2017).

[37] G. I. Taylor, VIII. stability of a viscous liquid contained between two rotating cylinders, Philos. Trans. R. Soc. London A **223**, 289 (1923).

[38] P. G. Drazin and W. Reid, *Hydrodynamic Stability* (Cambridge University Press, Cambridge, UK 2004).

[39] J. A. Müller, R. S. Stein, and H. H. Winter, Director dynamics of uniformly aligned nematic liquid crystals in transient shear flow, Rheol. Acta **33**, 473 (1994).

[40] T. Tsuji and A. D. Rey, Orientation mode selection mechanisms for sheared nematic liquid crystalline materials, Phys. Rev. E **57**, 5609 (1998).

[41] E. A Coddington and N. Levinson, *Theory of Ordinary Differential Equations* (Tata McGraw-Hill Education, New York, 1955).

[42] M. C. Calderer, C. Garavito, and C. Luo, Liquid crystal elastomers and phase transitions in actin rod networks, SIAM J. Appl. Math. **74**, 649 (2014).

[43] P. Dalhaimer, D. Discher, and T. C. Lubensky, Crosslinked actin networks show liquid crystal elastomer behaviour, including soft-mode elasticity, Nat. Phys. **3**, 354 (2007).

[44] R. Shangraw, W. Grim, and A. M. Mattocks, An equation for non-Newtonian flow, Trans. Soc. Rheol. **5**, 247 (1961).